Surface reactivity of Li2MnO3: Structural and morphological impact

Ambroise Quesne-Turin, Delphine Flahaut, Germain Vallverdu, Laurence Croguennec, Joachim Allouche, François Weill, Michel Ménétrier, Isabelle Baraille

Surface reactivity of Li_2MnO_3: structural and morphological impact

Ambroise Quesne-Turin[1,2,3], Delphine Flahaut[1,3], Germain Vallverdu[1,3*], Laurence Croguennec[2,3,4], Joachim Allouche[1], François Weill[2,3,4], Michel Ménétrier[2,3] and Isabelle Baraille[1,3]*

[1] CNRS/Univ. Pau & Pays Adour / E2S UPPA, Institut des Sciences Analytiques et de Physicochimie pour l'Environnement et les Matériaux − UMR 5254, 64000 Pau, France

[2] CNRS, Univ. Bordeaux, Bordeaux INP, ICMCB UMR 5026, F-33600 Pessac, France

[3] RS2E, Réseau Français sur le Stockage Electrochimique de l'Energie, FR CNRS 3459, F-80039 Amiens Cedex 1, France

[4] ALISTORE-ERI European Research Institute, FR CNRS 3104, F-80039 Amiens Cedex 1, France.

Corresponding authors

Delphine Flahaut

*E-mail: delphine.flahaut@univ-pau.fr.

Univ, Pau & Pays Adour / E2S UPPA, Institut des Sciences Analytiques et de Physicochimie pour l'Environnement et les Matériaux – UMR 5254, 64000 Pau, France

+33 540175006

Germain Vallverdu

*E-mail: germain.vallverdu@univ-pau.Fr

Univ, Pau & Pays Adour / E2S UPPA, Institut des Sciences Analytiques et de Physicochimie pour l'Environnement et les Matériaux – UMR 5254, 64000 Pau, France

+33 5 59 40 78 51

Abstract

This paper investigates the role of the stacking fault (5%, 20% and 50%) and the morphology of Li_2MnO_3 lamellar materials, issued from coprecipitation method with three annealing temperatures, on the surface reactivity. The structure and the morphology have been characterized by XRD, SEM and TEM. We studied the surface reactivity of these materials by combining X-ray photoemission spectroscopy (XPS), gaseous adsorption and first-principle calculations. An evolution of the reactivity toward the SO_2 acid gaseous probe has been observed for the three materials, from pure redox mechanism toward mixed acid-base/redox mechanisms, respectively for 5% and 50% of stacking faults. We demonstrated that the electronic structure of Li_2MnO_3 being not modified by stacking faulted. Thus, the surface reactivity of faulted Li_2MnO_3 is not linked to the SF rate but only governed by the accessible crystalline surfaces and the manganese environments at the surface atomic layer. The formation of (001)-Li surface according to the Li-overstoichiometry on the extreme surface and the random particles shape of the more faulted materials are responsible of the reactivity tuning.

Keywords

Surface reactivity, Li_2MnO_3, chemisorption, Li-ion battery, stacking fault,

1. INTRODUCTION

The layered oxide $LiCoO_2$ is still the mostly used material as positive electrode in commercialized lithium-ion batteries[1]. In order to circumvent its toxicity issues and the high cost of cobalt, other compositions of layered oxides were proposed. The best alternatives are nowadays the so-called NMC (333) ($LiNi_{1/3}Mn_{1/3}Co_{1/3}O_2$) and NMC (622) ($LiNi_{0.6}Mn_{0.2}Co_{0.2}O_2$) which exhibit a better cyclability than $LiCoO_2$ and a large capacity up to 185 $mAh.g^{-1}$,[2] with the upper voltage limited to 4.5 V vs Li^+/Li, instead of 140 $mAh.g^{-1}$ for $LiCoO_2$, with the upper voltage limited to 4.2 V vs Li^+/Li. The substitution of nickel and manganese for cobalt in $LiCoO_2$ (one Ni^{2+} and one Mn^{4+} for two Co^{3+}) results in (i) a lower cost, (ii) a higher thermal stability in the charge state of the battery thanks to a large fraction of Mn^{4+} in the framework, and (iii) the exchange of two electrons per transition metal from Ni^{2+} to Ni^{4+}.[3,4] The efficiency of such materials (i.e. NMC) is still limited by parasitic reactions which may occur at the electrode-electrolyte interface and lead, among other phenomena, to partial dissolution of the transition metals in the electrolyte[5]. Therefore, an improved knowledge of the surface properties and especially of the surface reactivity of these materials is crucial in order to understand the underlying mechanisms and propose solutions.

Only few surface reactivity studies have been carried out on $LiMO_2$ [6,7] or $LiCoO_2$. [8,9] Dahéron et al. [8] provides significant knowledge on the characterization of (001) $LiCoO_2$ surface and especially put in evidence, both by XPS and theoretical calculation, the existence of oxygen atoms from the extreme surface significantly different from the ones of the lattice. Thus, using an original method, developed in our group, based on the adsorption of gaseous probes at the extreme surface of the electrode material, monitored by X-ray photoemission spectroscopy (XPS) and coupled to first-principle calculations, Andreu *et al.* [6,10] investigated

the surface reactivity of $LiCoO_2$ and NMC, bare or coated by Al_2O_3. The coating was shown first to form an interphase[9], a substituted Al-layered oxide, at the interface between the coating Al_2O_3 and the active material $LiMO_2$, and then to decrease the surface reactivity toward the gaseous probes and changes the nature of the adsorbed species[9]. Following the same strategy, we recently focused on the role of manganese oxidation states on the surface reactivity through the investigation of $Li_2Mn^{4+}O_3$ and $LiMn^{3+,4+}{}_2O_4$ materials [11,12]. Depending on the nature of the manganese species present at the extreme surface of the material, Mn^{3+} and/or Mn^{4+}, acid-base and/or redox type reactivity is involved at the surface. Li_2MnO_3 being a Li^+ and Mn^{4+} rich layered oxide (also described as $Li[Li_{1/3}Mn^{IV}{}_{2/3}]O_2$) with lithium in excess in the transition metal layers,[13] it is particularly suitable as a model for understanding the surface reactivity of the high energy Li and Mn-rich layered oxides (the so-called HE-NMC's) expected to be the next generation of positive electrode materials for Lithium-ion batteries as they deliver high reversible discharge capacity involving both cationic and anionic redox.[14–16] Moreover, we have to mention that the particle size, Li-Mn site mixing and stacking fault content, controlled by the synthesis route[17], impact the electrochemical performances[18,19]. Menon *et al.*[18] explained that stacking fault and cation mixing are thought to facilitate the formation of long 3D Li percolation pathways responsible of larger charge/discharge capacity.

In a previous study, we studied the characteristic of the (001) surface of a Li_2MnO_3 crystal containing 50% of stacking fault[11]. Thus, in this paper, we choose to get even deeper understanding of the surface reactivity of Li_2MnO_3 by investigating the role of the morphology moving from crystals to powders showing a wide range of specific surface areas and stacking faults by controlling the annealing temperature. The reactivity has been

investigated by combining gas probe adsorptions and XPS characterizations associated to first principle calculations of the electronic structure of the compounds at their surface.

2. MATERIALS AND METHODS

2.1. Synthesis of the materials

The coprecipitation route was used to synthetize Li_2MnO_3 materials. A solution of $Mn(NO_3)_2$ (1M) (98% Fluka) was dropped into a solution of LiOH (1M) (98% Alfa Aesar) / NH_4OH (3M) (28-30% J.T. Backer) with a stoichiometric ratio such as Li/Mn is equal to 2. The precipitate was dried using a rotavapor at 80°C then heated at 650°C for 12 h. The material was grinded and heated a second time at 650°C, 750°C and 850°C for 24 h. The samples have been labeled LMO-SF based on the amount (in %) of stacking faults (SF) determined by XRD as discussed hereafter. These three samples were obtained at 850°C, 750°C and 650°C with 5%, 20% and 50% of SF respectively and will be called in the following LMO-5, LMO-20 and LMO-50, respectively.

2.2. Characterization of the structure, composition and morphology

The X-ray Diffraction (XRD) **patterns** were collected on a PANalytical Empyrean diffractometer, in reflection mode, with the copper radiation ($K_{\alpha1}$ = 1.5406 Å and $K_{\alpha2}$ = 1.5444 Å) and in the [8-75°] angular range with a counting time of 60 s and a 2θ step-scan intervals of 0.02°. The amount of stacking faults in each compound was determined considering the extended study performed by some of us few years ago, [17,20] to identify the nature of the stacking faults observed in Li_2MnO_3 and their impact on the X-ray diffraction pattern. Indeed, for significant contents of stacking faults, the overall structure can no more be

described by an average unit cell, and thus the X-ray diffraction pattern cannot be simply calculated by Le Bail and Rietveld type refinements. Simulations or calculations taking into account the formation of faults in the ideal structure have to be performed to fully explain the pattern and the actual structure. [17, 20-22] Here, in order to get a qualitative determination of the stacking faults' ratio, sufficient for the properties we wanted to address, we compared the X-ray diffraction patterns recorded in similar conditions to results previously obtained by some of us. [17,20]

Electron diffraction patterns were recorded on a JEOL transmission electron microscope (JEOL 2100) operated at 200kV and equipped with an Orius 200D camera from GATAN. Prior to the observation a suspension of the materials was obtained by grinding them in ethanol. A drop of the suspension was deposited on a carbon supported grid.

Inductively Coupled Plasma – Optical Emission Spectrometry (ICP-OES): The Li/Mn ratios have been determined using an inductively coupled plasma optical emission spectrometer (ICP-OES, Varian, 720-ES), after dissolving the samples in a HCl/HNO_3 acidic solution under boiling conditions.

Scanning Electron Microscopy (SEM): Scanning electron microscopy (SEM) analysis of metallized samples (Pd-deposited) was performed using a Hitachi Model S-4500 microscope.

Specific surface determination: Materials specific surface determination was performed by a Micromeritics ASAP 2010, using the Brunauer–Emmett–Teller (BET) theory[22]. We used a N_2 gas flux as adsorption gas, and worked at 77.300 K. The detection limit of this device is 1 m^2/g.

2.3. Surface investigation.

X-ray Photoelectron Spectroscopy (XPS): XPS analyses were performed on a Kratos Axis Ultra spectrometer with a focused monochromatized Al Kα radiation. The samples were fixed with double-coated tape and introduced in the spectrometer using an intermediate glove box to prevent any contamination or degradation of the adsorbed species due to a possible reactivity with the air. The vacuum in the analysis chamber was 5 x 10^{-9} mbar. The accelerating voltage and the applied current were 12 kV and 12 mA. The core peaks spectra have been calibrated by fixing the O 1s peak at 529.7 eV. After gas probe adsorption, due to the ultra-vacuum conditions of XPS analyses, only chemisorbed species are detected. According to the weak interactions involved, physisorbed species are supposed to undergo a quick desorption. Considering the size of the particles analyzed as it will be discussed in the following, the size of the XPS spot (700 x 400 μm) ensures that all the faces are statistically analyzed.

Gas probe adsorption: The adsorption experiments were performed in a Micromeritics Autochem analyzer. 0.1g of samples was disposed onto a stainless frit in the reactor, previously cleaned and heated at 500°C under argon flux for 1h. The first step consisted in preparing the sample surface by heating the sample at 350°C for 4h under an argon flux, to remove all the physisorbed species from the surface. In a second step, the temperature was decreased to 80°C and the sample submitted to a helium flux for 1h. Then, to perform the probe adsorption, the gas was switched to a blend of 0.02% SO_2 in helium for 15 min while maintaining the temperature at 80°C. The final step consisted in cleaning the surface of physisorbed species under a helium flux at 80°C for 1h. This whole procedure was performed three times to ensure the reproducibility of our results.

The SO_2 gaseous probe allows the investigation of acidic-basic and redox properties. This probe was chosen because of its rather strong acidity and its small size, which allow to access to the largest amount of surface active sites. Moreover, sulfur is not present in the pristine materials and exhibits a large XPS binding energy (B.E.) scale suitable for the identification of the adsorbed species. Indeed, a reaction between SO_2 and one oxygen atom of the extreme surface leads to the formation of a sulfite species (SO_3^{2-}), characterized by an S $2p_{3/2}$ core peak binding energy at 167.5 eV [10], whereas its reaction with two extreme surface oxygen atoms leads to the formation of sulfate species (SO_4^{2-}) characterized by an S $2p_{3/2}$ core peak binding energy at 169 eV [10]. Finally, the interaction of the sulfur atom with a metal from the surface by dissociative mechanism results in the formation of sulfide species (S^{2-}) (B.E. (S $2p_{3/2}$) ≈ 162.0 eV) [23,24]. The nature and the amount of adsorbed species were characterized by X-Ray photoelectron spectroscopy analyses.

2.4. Computational details

The electronic structure is calculated from density functional theory (DFT) calculations in 2D or 3D periodic boundary conditions for surface and bulk systems respectively. All the calculations were performed with the Vienna Ab initio Simulation Package[25,26] (VASP) with the revised version for solid of the Perdew Burke Enrzerhoh (PBE) functional[23]. The wave-functions were described in the Projector Augmented Wave[27,28] (PAW) formalism with a plane waves basis set truncated at a cut-off energy of 600 eV to reach a convergence of 10 meV per atom. Valence electrons described explicitly in the calculations were $1s^2 2s^1$, $4s^2 3d^5$ and $2s^2 2p^4$ for lithium, manganese and oxygen atoms respectively. The Brillouin zone integration was done on a k-points grid uniformly distributed around the origin (Γ point) using a spacing of 0.35 $Å^{-1}$ corresponding to a mesh of 4 × 3 × 4 for the $C_{2/m}$ bulk structure of

Li_2MnO_3. For the density of states (DOS) calculations the k-point mesh was multiplied by a factor 5. Charges calculations were performed by using Bader's topological analysis[29] on the basis of a finer grid for the density with a step of 0.03Å. For 3D calculations, the atomic positions were relaxed first and then all degrees of freedom were fully relaxed until forces are lower than 0.01 $eV.Å^{-1}$. For 2D calculations, only the atomic positions were relaxed using the lattice parameters obtained from bulk calculations for the periodic directions.

All calculations were done considering spin polarization with a ferromagnetic ordering. The magnetic moments of each atom were computed from the difference between spin up and spin down electronic densities. In order to describe accurately the strongly localized 3d electrons of manganese atoms, DFT+U calculations were undertaken using the rotationally invariant approximation of Dudarev *et al.*[30] using a single effective parameter U_{eff} = 5 eV which was determined for Mn^{4+} species[31] and commonly used for lithium layered oxides with manganese atoms[32,33].

3. RESULTS

3.1. Structure, morphology and composition

The X-ray diffraction patterns of the three Li_2MnO_3 samples synthesized in this work are compared in Figure 1. As already explained in the experimental part, the stacking faults ratios were estimated to 5, 20 and 50%, by comparison with results reported by some of us [17].

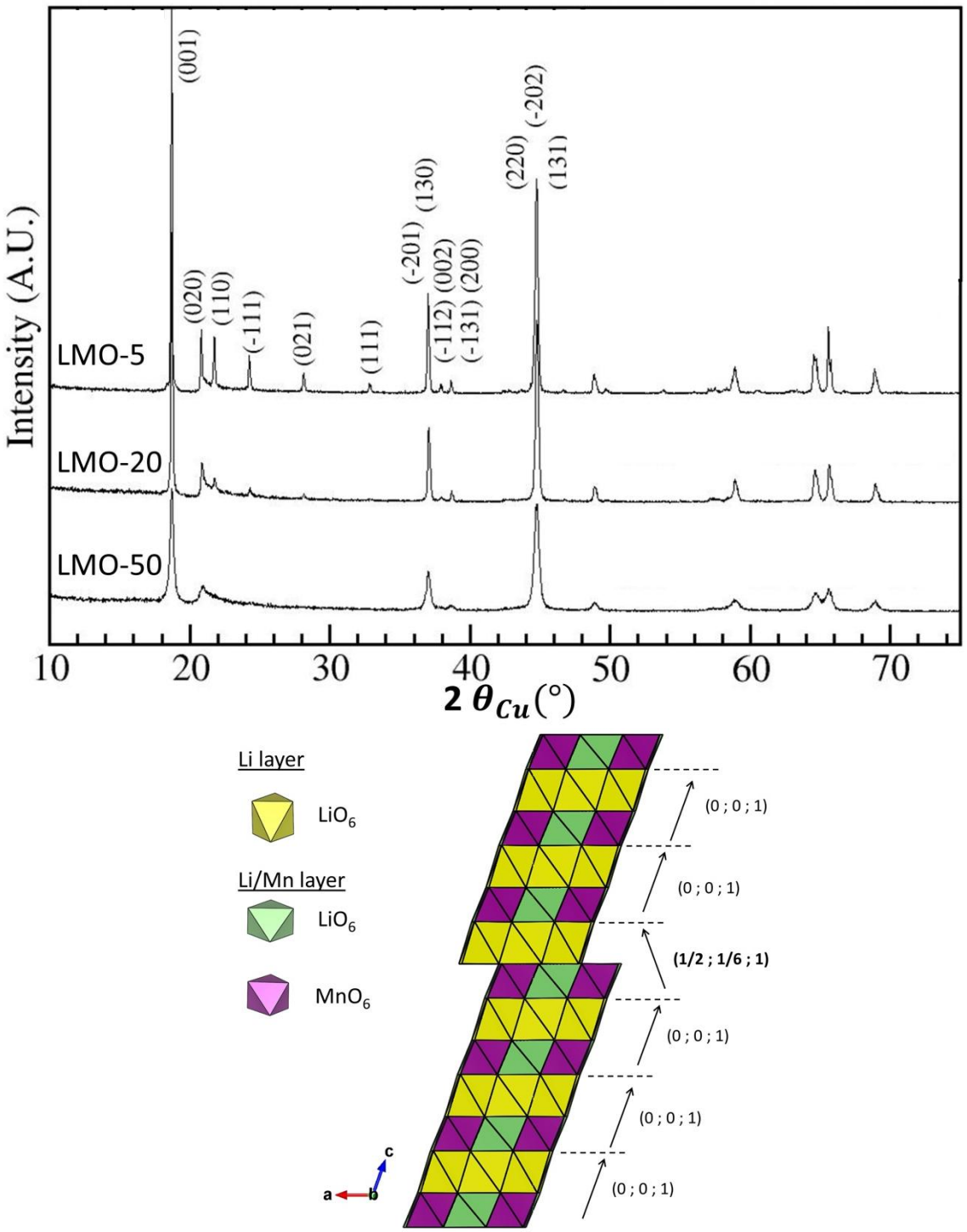

Figure 1. Comparison of the XRD patterns obtained for the three Li_2MnO_3 samples with different stacking faults ratios: LMO-SF with SF = 5, 20 and 50, determined by comparison with results reported by Boulineau *et al*[17](see Figure S2 in supplementary information) (up).

Structure of Li_2MnO_3 with a stacking fault and the corresponding vector. Only octahedra are represented in yellow, green and violet for LiO_6 in lithium layer, LiO_6 and MnO_6 in the lithium manganese layer, respectively (down).

All the diffraction lines can be indexed using a unit cell described in the monoclinic space group $C_{2/m}$, with cell parameters a ≃ 4.929 Å, b ≃ 8.531 Å, c ≃ 5.025 Å and β ≃ 109.34°. Note that depending on the synthesis conditions, the (020), (110), (-111), (021) and (111) peaks observed in the 20°-34° (2θ) angular range reveal a significant difference in broadening, which is huge for the sample LMO-50 obtained after a thermal treatment at lower temperature (650°C). These diffraction lines are the signature of the ordering between the Li^+ and Mn^{4+} ions in the octahedral sites of the slabs $[Li_{1/3}Mn_{2/3}]O_2$, and of their ordered stacking along the c_{axis}. The anisotropic broadening of these reflections (i.e. a diffuse asymmetry) is mainly associated to the presence of faults in the stacking of the ordered slabs $[Li_{1/3}Mn_{2/3}]O_2$ along the $\vec{c}_{axis}$. [17] Indeed, the stacking vector is expected to be (0; 0; 1) whereas, as explained by Lang and Bréger, [34,35] two others, (1/2; 1/6; 1) and (1/6; 1/6; 1), corresponding to an in-plane gliding of the metal layer (see Figure 1) can occur, with an occurrence probability depending on the annealing temperature. The higher the annealing temperature, the sharper the diffraction lines are and the smaller the amount of stacking faults is. Indeed, the line profile required to describe the lines (020), (110), (-111), (021) and (111) observed for LMO-5 is close to that used for the overall pattern showing that the structure of Li_2MnO_3 is close to an extended ordered structure, in the $[Li_{1/3}Mn_{2/3}]O_2$ slabs between the Li^+ and Mn^{4+} ions and along the c_{axis} in the stacking of these ordered slabs. Nevertheless, the asymmetry of the (020)

line highlighted by the high background between the (020) and (110) diffraction lines reveals the residual presence of a small amount of stacking faults.

To support these results obtained by XRD analysis, electron diffraction has been performed on the three materials. Typical electron diffraction patterns are reported in Figure 2. All of them were obtained along the [110] zone axis which allows to visualize how far from ideal the stacking of the layers is. In all these patterns the central direction corresponds to the c* direction. Lines parallel to this direction are observed. The third one from the center is always similar to c* as corresponding to a direction of the basic cell describing the classical layered oxide compounds (i.e. $LiMO_2$ without any ordering within the slabs and thus along the c_{axis}). The two first lines are on the contrary related to the stacking sequence induced by the Li^+ and Mn^{4+} ordering in Li_2MnO_3: the more diffuse they are the higher is the number of stacking faults. Obviously, on the diffraction pattern corresponding to LMO-50 only diffuse lines are observed between the rows of spots corresponding to the basic structure: their presence supports the ordering within the slabs of Li_2MnO_3 but the extended diffusion reveals the presence of a large amount of stacking faults along the c_{axis} and thus the quasi absence of correlation between the ordered slabs. On the other hand, despite residual diffusion the reflections corresponding to the monoclinic structure are clearly observed on the two first lines of the patterns corresponding to the two other compounds, LMO-20 and LMO-5, indicating the presence of a smaller amount of stacking faults.

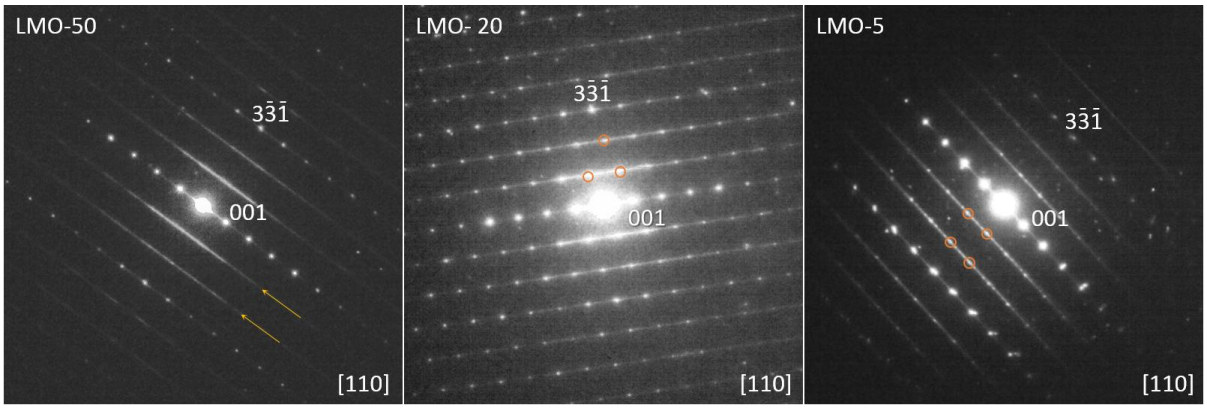

Figure 2: Electron diffraction patterns recorded along the [110] zone axis and representative of the compounds LMO-50, LMO-20 and LMO-5. The two yellow arrows on the LMO-50 pattern indicate diffusion lines revealing a high degree of stacking faults. The circles on the LMO-20 and LMO-5 patterns highlight the presence of reflections associated to the monoclinic structure and to the extended ordered structure of Li_2MnO_3.

The Li/Mn ratios have been determined by chemical analyses using ICP-OES. The actual compositions are found very close to the expected ones, considering the stoichiometry in oxygen is equal to 3: $Li_{2.01(\pm0.05)}Mn_{1.00(\pm0.04)}O_3$ for the LMO-5 material, $Li_{2.02(\pm0.05)}Mn_{1.00(\pm0.04)}O_3$ for the LMO-20 material and $Li_{1.99(\pm0.05)}Mn_{1.00(\pm0.04)}O_3$ for the LMO-50 material (Table 1). Any direct correlation can thus be made between the average stoichiometry and the amount of stacking faults.

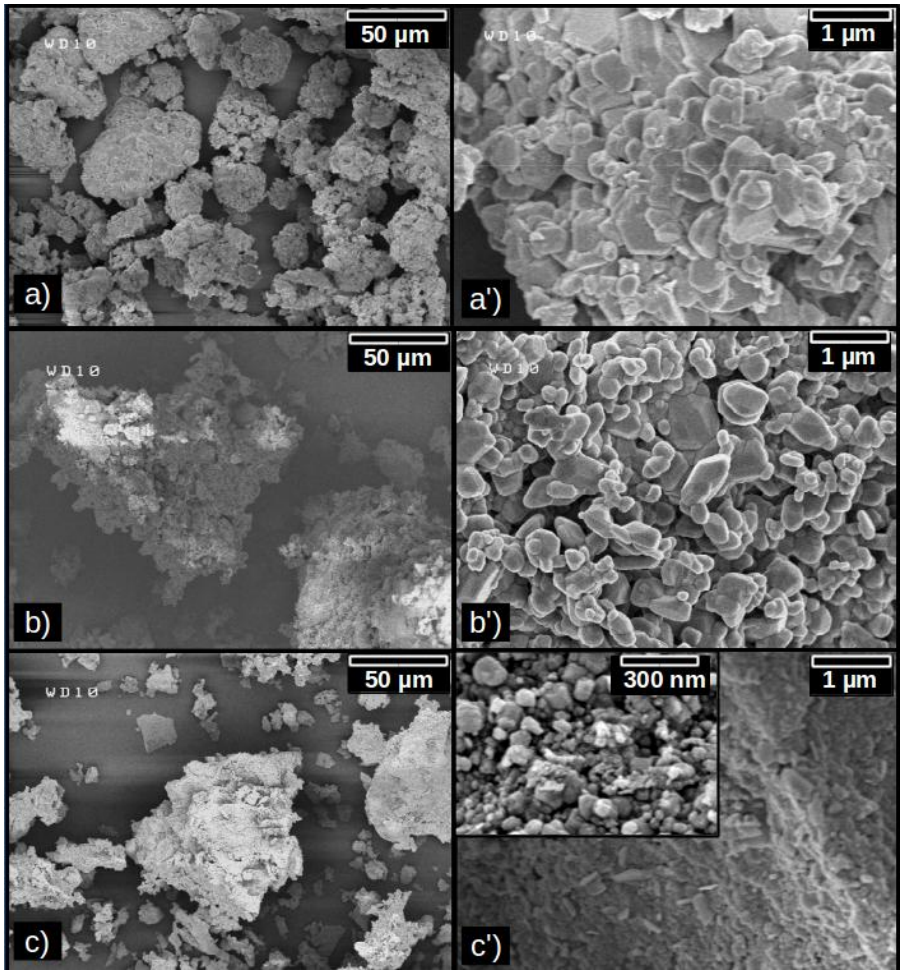

Figure 3. SEM images of the three Li_2MnO_3 samples: a) and a') LMO-5, b) and b') LMO-20, c) and c') LMO-50.

As shown by the SEM images (Figure 3), the three samples are characterized by agglomerates of primary particles. These agglomerates reveal heterogeneous shapes and sizes ranging from 1 µm to a few hundred µm, whereas the primary particles size strongly depends on the synthesis parameters: the higher the annealing temperature, the larger the particles are. Note that the specific surface area increases significantly from 1.57 (± 0.02) $m^2.g^{-1}$ for LMO-5 to 6.36 (± 0.05) $m^2.g^{-1}$ for LMO-50. In parallel, the analysis of the XRD patterns has also shown that the higher the annealing temperature, the smaller is the amount of stacking faults. In our

synthesis conditions and for the materials studied, a lower synthesis temperature is thus associated with smaller particles size and higher specific surface area (as expected) and a higher amount of stacking faults (Table 1). But, it does not imply that particles size and amount of stacking faults are correlated: indeed, a stacking fault is spread within the crystal (in the bulk) and thus not observed at the surface only, as defects could be for instance.

Samples	**LMO-5**	**LMO-20**	**LMO-50**
Stoichiometry	$Li_{2.02\ (\pm 0.01)}Mn_{1.00\ (\pm 0.04)}$	$Li_{2.02\ (\pm 0.05)}Mn_{1.00\ (\pm 0.04)}$	$Li_{1.99\ (\pm 0.05)}Mn_{1.00\ (\pm 0.04)}$
% SF	< 5	20	50
Particles' length (nm)	550	300-500	10-100
SA ($m^2.g^{-1}$)	1.57 (± 0.02)	2.53 (± 0.01)	6.36 (± 0.05)

Table 1. Composition in Li and Mn, amount of stacking faults (% SF), particles size and specific surface area (SA) of the Li_2MnO_3 samples.

3.2. Surface characterization by XPS of the bare Li_2MnO_3 materials

First, the bare materials were considered and their surface properties characterized by XPS analyses. The XPS core peaks Mn 2p, Mn 3s, O 1s, and Li 1s and C 1s (given in supplementary information as Figure S3 and S4) of the three LMO samples have been recorded before gas probe adsorption. The Mn 2p and Mn 3s core peaks are depicted in Figure 4. The binding energy values of the Mn $2p_{1/2}$ (654.3 eV) and Mn $2p_{3/2}$ (642.3 eV) main components as well as the splitting B.E. value of the Mn 3s core peak (4.5 eV-4.2 eV) are characteristic of tetravalent manganese atoms in an oxygenated environment[11,12]. As no shoulder has been observed at 641.4 eV[11], the presence of Mn^{3+} cations could be excluded. Moreover, the value of the Mn 3s multiplet splitting is 4.5 eV and no significant change has been detected for the three S.F. ratio values. Thus, we could confirm that the presence of

manganese at the trivalent and divalent states can be excluded as the Mn 3s core peaks splittings would be of 5.5 eV and 6.5 eV, respectively.[36]

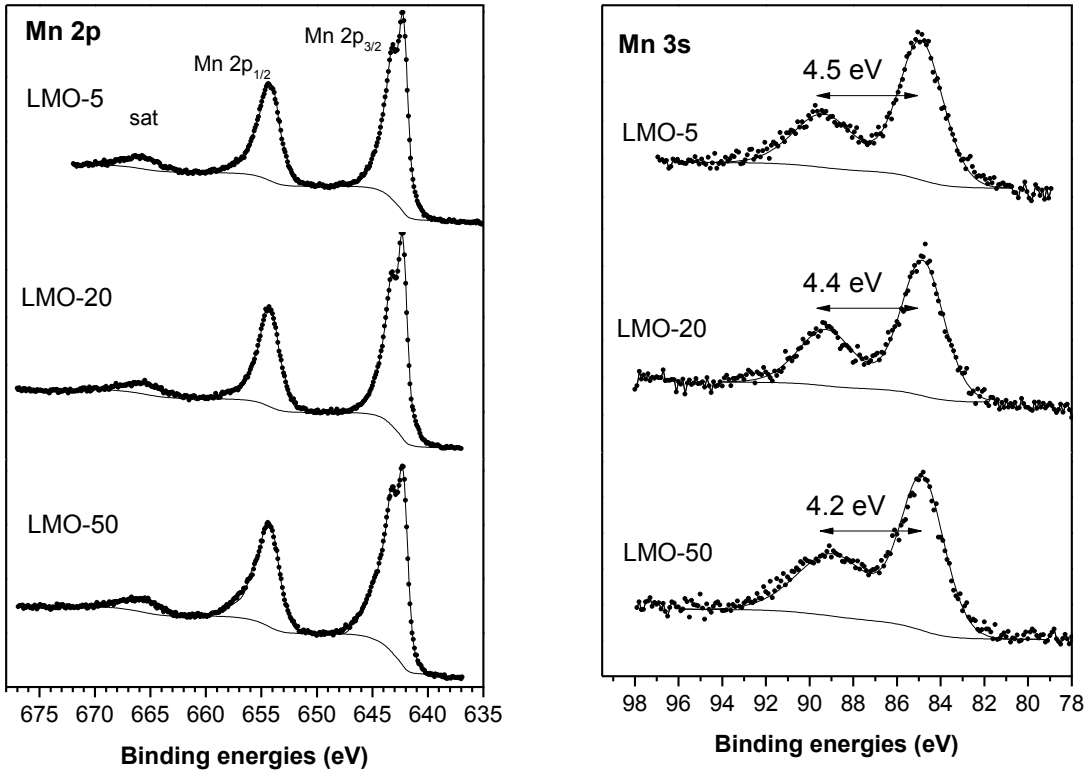

Figure 4. Mn 2p (left) and Mn 3s (right) core peaks for Li_2MnO_3 materials characterized by different contents in stacking faults (S.F.).

The Li 1s spectra (given in supplementary information as Figure S3) exhibit, whatever the content in SF, a unique component localized at 54.5 eV and associated to Li^+ in Lithium layered oxides[6]. No components characteristic of Li_2CO_3 (B.E. C 1s = 290.1 eV and Li 1s = 55.5 eV) and LiOH (B.E. Li 1s = 54.9 eV)[37], usual impurities formed on the Li transition metal oxides surfaces, have been identified. According to the atomic percentages determined from the analysis of the XPS spectra and gathered in Table 2, the samples LMO-5 and LMO-20 are underlithiated. Indeed the Li 1s / Mn 2p ratios are of 1.5 and 1.7 respectively, whereas

the expected ratio is 2. On the contrary, the LMO-50 sample appears overlithiated with a Li/M ratio at its surface of 2.5. However, we have obtained by considering the Mn 3p signal, that the Li 1s / Mn 3p ratio values are lower, 0.6, and constant for these three samples. The binding energies of the Mn 3p core peaks are closer to the Li 1s B.E. and much lower than for the Mn 2p. Thus, the Mn 3p core peaks are more assigned to the deeper analysis zone of the XPS than Mn 2p core peaks. Thus, the large difference in the Li / Mn ratio depending of the considering manganese orbitals could be related in part to the migration of the Lithium ion toward the surface. Moreover, as no change on the Mn 2p and Mn 3s spectra has been identified depending on the Li / Mn ratio, we thus could estimate that the manganese valence is almost three in the first ten nanometers of the material.

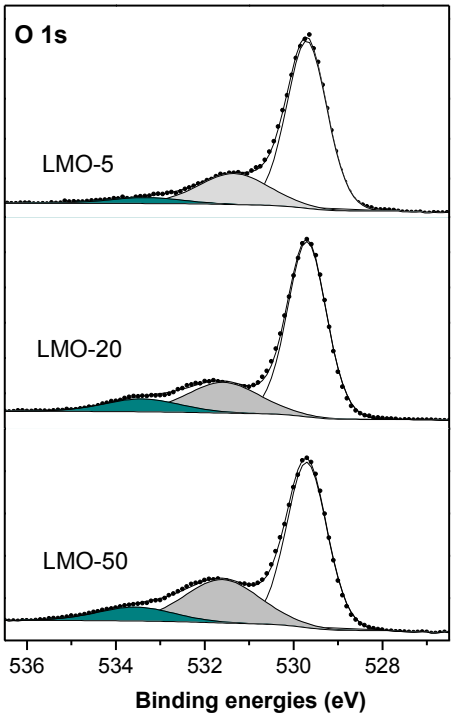

Figure 5. O 1s core peaks for the three Li_2MnO_3 samples with 5%, 20% and 50% of stacking faults before adsorption. The white, grey and green components correspond to the structural oxygen atoms, the surface oxygen atoms and the oxygen atoms of adsorbed species, respectively.

The O 1s spectra reported in Figure 5 have been decomposed into three components. The first one at 529.7 eV is associated to the oxygen anions in the bulk of the lithium layered oxides, the second one at 531.4 ± 0.2 eV is assigned to the oxygen anions localized at the extreme surface of the lithium layered oxides and showing a deficient coordination[12], and the last one at 533.4 ± 0.2 eV is attributed to the oxygen atoms issued from adsorbed species. A slight increase of the proportion of surface oxygen atoms and adsorbed species (at 531.6 and 533.7 eV) is observed in Figure 5, from 28% to 38% of the whole O 1s signal for LMO-5 and LMO-50 respectively, which is consistent with the increase of the specific area of these materials.

		LMO-5		LMO-20		LMO-50	
		B.E. (eV)	**At. %**	**B.E. (eV)**	**At. %**	**B.E. (eV)**	**At. %**
Mn 2p		642.3	**15.6**	642.3	**10.6**	642.3	**10.6**
O 1s	Adsorbed species	533.3	1.8	533.4	3.6	533.6	3.2
		531.3	9.6	531.6	8.2	531.6	10.0
	O^{2-}	529.7	29.9	529.7	25.4	529.7	20.6
			41.4		**37.2**		**33.8**
C 1s	CO_2	288.9	3.9	288.9	3.0	288.9	4.0
	C-O	286.8	2.4	286.5	3.8	286.6	7.6
	C-C, C-H	285.3	10.6	285.1	27.8	285.2	17.6
			15.0		**34.7**		**29.2**
Li 1s		54.5	**24.2**	54.5	**17.5**	54.5	**26.4**
Li/Mn 2p			**1.5**		**1.7**		**2.5**
Li/Mn 3p			**0.6**		**0.6**		**0.7**

Table 2: Binding energies (eV) and atomic percentages (at.%) determined for the Mn, O, C and Li elements from the analysis of the XPS spectra recorded for the three LMO-SF (SF = 5, 20 and 50) samples, before adsorption.

Electronic structure of perfect and faulted structures

The electronic structure of a bulk Li_2MnO_3 was investigated from DFT+U calculations[11, 32, 33]. The full relaxation of the $C_{2/m}$ unit cell of Li_2MnO_3 leads to the lattice parameters a = 4.94 Å, b = 8.54 Å, c = 5.01 Å and β = 109.5°. The highest relative deviation from the experimental lattice parameters is obtained for the parameter c with 0.5%. Li and Mn atoms contained in Li_2MnO_3 are partially disordered in the transition metal layers. However, in our study, we decide to only consider the effect of stacking faults on the electronic structure on an ideal material structure, without atomic mixing. In order to investigate the impact of SF on the bulk structure, 1×1×2, 1×1×3 and 1×1×4 supercells were built. In each cell a Li/Mn plane was shifted according to the (1/2, 1/6) vector. These three structures are in fact associated to 50%,

33% and 25% of stacking faults respectively. Only a difference in energy of 0.5 meV per formula unit is observed for the three structures in comparison with the perfect stacking described in the $C_{2/m}$ space group. This value being in the range or below the accuracy of the calculation, it leads that the energy cost for the formation of SF is close to zero which agree with the existence of this kind of faults. After the full relaxation of the structure geometry, whatever the amount of SF the first coordination spheres of Mn and Li remain unchanged, the Mn-O and Li-O bond lengths being 1.92 Å and 2.05 Å, respectively. The comparison of the electronic structures of bulk and faulted systems was done by comparing the density of states (DOS) and the electronic potential energy. The computed DOS of the perfect bulk system and the SF50 model are superimposed, see Figure S5. In Figure S6 we have projected the average electrostatic potential energy along the c-axis for the perfect and SF50. One can see that the electrostatic potential energy curves are superimposed and that the periodicity of the potential energy is not broken due to the stacking fault. Thus, we confirmed that the different electrochemical performances reported for Li_2MnO_3 materials containing different S.F. content and exhibiting different morphology[18] are not directly linked to stacking fault content and Li/Mn ordering.

3.3. Surface characterization by XPS of Li_2MnO_3 after SO_2 adsorption

The surface reactivity of LMO-SF materials was investigated by coupling the adsorption of SO_2 as a gas-phase probe and XPS analyses, under controlled conditions, by considering in detail all the core peaks associated to the elements of the materials and of the adsorbed species.

The stoichiometry and the electronic structure at the materials' surface have been checked by XPS just after the first step of the adsorption procedure. Based on the quantitative analysis,

we have evidenced that the thermal treatment increases the surface Li over-stoichiometry, i.e. Li/Mn 2p (Table 3) are increasing after adsorption for the three samples, and that the Li/Mn 2p evolution versus the S.F. content is maintained. This may be due to the combine effect of the increase of the specific surface (with the SF rate) and a migration of the Li ion toward the surface during the adsorption process related to its huge reactivity.

The S 2p core peaks associated to the adsorbed gas probe are shown in Figure 6. The atomic percentages of all the elements present at the surface are gathered in Table 3. Concomitantly, the O 1s core peaks spectra given in figure 7 present a significant increase in the amount of the surface oxygen species after SO_2 adsorption, in agreement with the additional contribution of oxygen from the adsorbed SO_2 gas probe.

The concentration of adsorbed species is of the same order of magnitude as on the Li_2MnO_3 crystal surface (S/M = 0.1) reported by Flahaut et al.[8] In the case of LMO-5, a sole S 2p doublet is observed with a S $2p_{3/2}$ B.E. of 169.0 eV characteristic of sulfate species[6]. For the LMO-20 and LMO-50 samples, a second environment characteristic of sulfite species is observed at S $2p_{3/2}$ BE of 167.6 eV and 168.0 eV, respectively. Thus, the two more faulted samples and large S.A. allow the adsorption of the SO_2 gas probe in the form of both sulfate and sulfite species. At first sight, the surface reactivity of the LMO-SF materials appears to be directly linked to the SF ratio and the particles size.

But, we notice that the total reactivity toward SO_2 decreases with the increase of the SF ratio concomitantly with the specific area. Indeed, the S/Mn 2p ratio decreases from 0.20 for LMO-5 to 0.10, for both LMO-20 and LMO-50, just as in the case of the proportion of the oxygen component, associated to the adsorbed species (B.E. = 531.3 eV), in the entire O 1s

signal. Thus, the SO_2 adsorption is less favor when the oxide anions are present in a lesser extent at the surface concomitantly with an increase of the Li over-stoichiometry.

The more faulted materials favor the acidbase adsorption mechanism as the sulfite contribution to the whole S 2p signal is of 13.8% and 30.6%, respectively, for LMO-20 and LMO-50. In addition, we can notice that the S $2p_{3/2}$ B.E. assigned to the sulfate species increases up to 169.5 eV for the LMO-50 material.

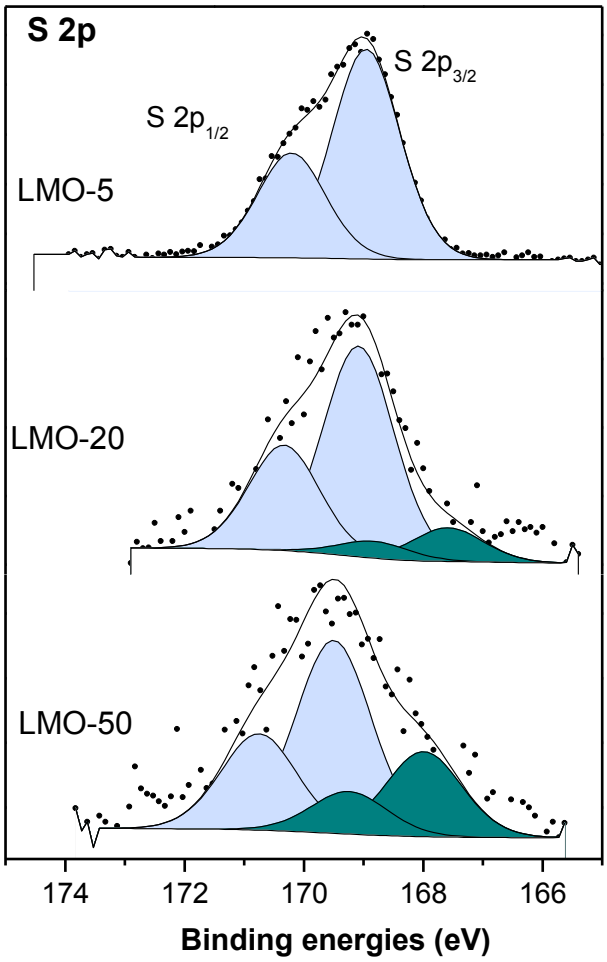

Figure 6. S 2p core peaks after adsorption for the three LMO materials.

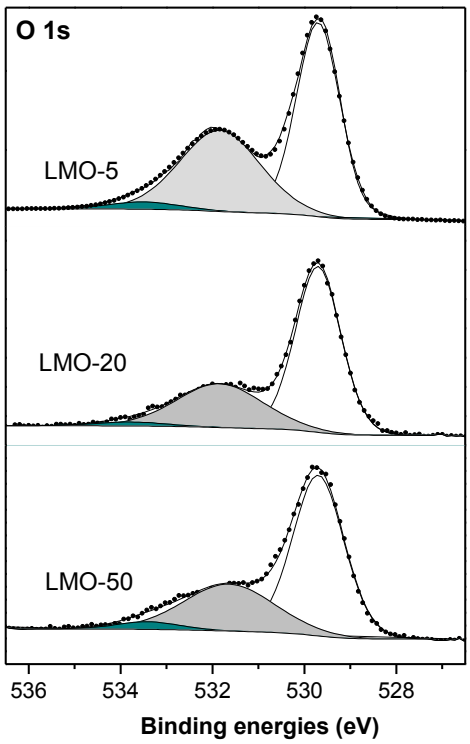

Figure 7. O 1s core peaks for the three Li_2MnO_3 samples with 5%, 20% and 50% of stacking faults after adsorption. The white, grey and green components correspond to the structural oxygen atoms, the surface oxygen atoms and the oxygen atoms of adsorbed species, respectively.

	LMO-5		LMO-20		LMO-50	
	B.E. (eV)	**At %**	**B.E. (eV)**	**At. %**	**B.E. (eV)**	**At. %**
Mn 2p	642.3	**11.7**	642.3	**9.7**	642.3	**9.5**
O 1s	533.5	5.1	533.8	2.8	533.9	2.1
	531.8	18.2	531.8	10.3	531.8	10.5
	529.7	23.8	529.7	20.6	529.7	19.1
		47.1		**33.6**		**34.3**
C 1s	289.2	0.8	288.7	2.0	288.6	1.9
	286.6	4.4	286.3	3.1	286.2	5.6
	285.0	8.5	285.0	22.3	284.8	20.9
		13.7		**27.5**		**28.4**
S $2p_{3/2}$	169.0	2.5	169.0	1.0	169.5	0.4
			167.6	0.2	168.0	0.3
		2.5		**1.2**		**0.7**
Li 1s	54.5	**25.0**	54.5	**28.0**	54.8	**27.5**
Li/Mn 2p		**2.1**		**2.8**		**2.8**
Li/Mn 3p		**0.6**		**0.6**		**0.6**

Table 3. Binding energies (eV) and atomic percentages (at. %) obtained from XPS analyses of LMO-SF materials with SF = 5, 20 and 50% and after SO_2 adsorption.

4. DISCUSSION

LMO materials showing different particle size, specific surface area and amounts of stacking faults were studied using XPS, before (as bare) and after SO_2 gas probe adsorption and DFT calculations. Clear and continuous differences have been observed between LMO-5, LMO-20 and LMO-50 samples. The higher the synthesis temperature, the larger are the particles size and the smaller amount of stacking faults is obtained: moving from LMO-50 to LMO-20 and LMO-5 synthesized at 650, 750 and 850°C respectively.

The adsorption of SO_2 gas probe at the surface of the three samples has revealed the formation of sulfate species for LMO-5 whereas both sulfate and sulfite species are formed on LMO-20 and LMO-50. The acidbase adsorption mode is favored for large SF ratio and small particles as the accessible oxide anion, needed to form sulfate species, at the extreme surface is decreasing due to the overstoichiometry in Lithium ions. According with the particles shape evolution with the stacking fault contents, we must also consider the role of the manganese environment and the surface index on the adsorption mode[11].

The LMO-5 particles being platelet like, their surfaces could be assigned to the most stable surface for the Li_2MnO_3 material, i.e. the (001)-O surface[32]. Previous theoretical studies[11,12] have demonstrated that this surface contains mainly Mn^{4+} cations and favors the formation of the sulfate species. These results can be directly compared to those obtained on LMO crystals oriented along the (001) direction. For this crystal, the surface reactivity was dominated by a redox adsorption mode characterized by a unique doublet with a BE of S $2p_{3/2}$ at 169.0 eV assigned to sulfate species, the same as in LMO-5. The comparison between the results on a (001) oriented platelet powder sample (LMO-5) and a crystal oriented along the (001) direction may state that, both, the (001)-O surface and the Mn^{+4}cations of LMO favors redox adsorption mode and sulfate formation. Moreover, as the SF ratio of the crystal reaches 50%, we can argue that the SF ratio cannot be retained to explain the tuning of the surface reactivity. This last point has been confirmed because of computational results that show that the electronic structure of LMO is not modified consequently to the introduction of a SF even on the sub-surface atomic layer. It should also be noted that the Li / Mn ratio are nearly equal, 1.4 for the crystal and 1.5 for LMO-5.

If we are looking for the LMO-20 and LMO-50 materials, the SEM images evidence that, the particles shape is getting more random with the increase of the surface area and the Li / Mn ratio. As the dispersity of the samples morphology get larger concomitantly with the Li-overstoichiometry, the orientation of the surfaces and thus the manganese atom environments are modified.

We suggest that the MnO_6 octahedron of a well-defined (001) surface could become MnO_x environments due to the loss of one or more Mn-O chemical bonds associated to the formation of surfaces of higher indexes[38]. This surface modification should promote other manganese valence states such as Mn^{3+} [11,12] on the top atomic layer, in a such very low content that could not be discernable by XPS. Thus, the acid-base adsorption mode[11] could be favored with the formation of sulfite species.

We could also suggest that the surface reactivity is governed by another parameter, which plays on the surface reactivity, the increase of the Li content at the surface. This hypothesis could match with the results issued from calculations on the (001)-Li surface for which the manganese atoms are still in the tetravalent state[11]. Both acid-base and redox (which involve a manganese surface reduction) modes are indeed thermodynamically favorable for the SO_2 adsorption mechanism on this surface (-2.1 eV and -1.7 eV, respectively, for sulfate and sulfite species). The increase of Li / Mn 2p involves also interaction between adsorbed species and Lithium as secondary interaction, which conduct to a preferential sulfite species adsorption[12]. The increase of sulfite species, reported in Figure 6, with the Li / Mn 2p ratio support this hypothesis.

It is to note that the S $2p_{3/2}$ B.E. values after SO_2 adsorption on the LMO-SF surfaces are slightly larger than those usually reported, in the case of the formation of sulfite and sulfate

species at the oxide materials surface, i.e. 167.5 eV and 169 eV [6,9,39], respectively. Theoretical studies [7,11] have provided a detailed view of the underlying electronic processes associated to the adsorption mechanism of the SO_2 gas probe on the Li_2MnO_3 and $LiMO_2$ (M = Ni, Mn, Co) surfaces using first-principle calculations. In the case of sulfite adsorption mode, an electronic transfer is observed from the surface toward the SO_2 molecule of about 0.4e whereas, no electronic transfer was observed in the case of $LiCoO_2$. Moreover, this electronic transfer is localized on the oxygen atoms surrounding the sulfur atom of the SO_2 molecule leading to an environment that becomes more negatively charged and could explain the increase of the B.E. of the S2p core peaks in that case. In the case of sulfate species, there is a clear shift of the S 2p core peaks toward higher BE. This shift is correlated to the Li/Mn ratio which is higher than all other surfaces investigated previously (Li/Mn = 1.4 in ref 11).

5. CONCLUSION

The surface reactivity of Li_2MnO_3 (LMO) material was investigated through the adsorption of SO_2 gaseous probes followed by XPS characterization. This material allows us to investigate the role of Mn atoms at the tetravalent state in the reactivity of NMC compounds. The materials were synthetized by a coprecipitation route and three samples showing an evolution in the morphology and stacking faults (SF) ratio were obtained with 5, 20 and 50% of stacking faults.

The adsorption mechanism of SO_2 the acid gas probe changes depending on the stacking fault content. However, calculations give the proof that the SF do not impact the density of states of the material. For platelets materials, the adsorption mode is redox. Indeed, the (001)-O surface is favored, while possessing Mn^{4+} cations and lower Li content at the extreme

surface. The SO_2 adsorption mechanism evolves toward an acidbase mode for the more faulted materials where the overstoichiometry in Li and the Mn^{4+} ions at the extreme surface leads to the formation of (001)-Li surface for which, both acidbase and redox mechanisms are favorable.

So, the parameters governing the adsorption mechanism and the tuning from redox toward acidbase adsorption are related, in a first instance, to the orientations of the power facets and the manganese electronic structure, and secondly to the Li/Mn ratio at the last surface layer. Thus, high faulted Li_2MnO_3 materials are less reactive toward acid probe while promoting Li 3D percolation pathway at the primary particles surfaces.

ACKNOWLEDGMENTS

The authors thank the Conseil Général des Pyrénées Atlantiques and the French Research Network on the Electrochemical Energy Storage (RS2E) for funding the AQT's PhD fellowship, and Philippe Dagault (ICMCB-Pessac) for his technical support. This project received also funding from Région Nouvelle Aquitaine and the French National Research Agency (STORE-EX Labex Project ANR-10-LABX-76-01). The theoretical calculations were performed using HPC resources from GENCI-CINES (Grant 2017 A0010806920) and the Mesocentre de Calcul Intensif Aquitain (MCIA).

REFERENCES

(1) K. Ozawa, Lithium-Ion Rechargeable Batteries with $LiCoO_2$ and Carbon Electrodes: The $LiCoO_2$/C System, Solid State Ion. 69 (3) (1994) 212–221.

(2) E. Rossen, C. D. W. Jones, J. R. Dahn, Structure and electrochemistry of $Li_xMn_yNi_{1-y}O_2$, *S*olid State Ion. 57 (3) (1992) 311–318; T. Ohzuku, Y. Makimura, Layered lithium insertion material of $LiNi_{1/2}Mn_{1/2}O_2$: A possible alternative to $LiCoO_2$ for advanced lithium-ion batteries. Chem. Lett., 30 (8) (2001) 744–745; H.-J. Noh, S. Youn, C.S. Yoon, Y.-K. Sun, Comparison of the structural and electrochemical properties of layered $Li[Ni_xCo_yMn_z]O_2$ (x = 1/3, 0.5, 0.6, 0.7, 0.8 and 0.85) cathode material for lithium-ion batteries. J. Power Sources 233 (2013) 121–130; Series on Chemistry, Energy and the Environment: Prospects for Li-ion Batteries and Emerging Energy Electrochemical Systems, pp. 57-104 (2018) Chapter 2: Li-Rich Layered Oxides: Still a Challenge, but a Very Promising Positive Electrode Material for Li-Ion Batteries by S. Pajot, L. Simonin and L. Croguennec

(3) W.-S. Yoon, C. P. Grey, M. Balasubramanian, X.-Q. Yang, D. A. Fischer, J. McBreen, Combined NMR and XAS Study on Local Environments and Electronic Structures of Electrochemically Li-Ion Deintercalated $Li_{1-x}Co_{1/3}Ni_{1/3}Mn_{1/3}O_2$ Electrode System. Electrochem, Solid-State Lett. *7* (3) (2004) A53–A55.

(4) W.-S. Yoon, M. Balasubramanian, K.-Y. Chung, X.-Q. Yang, J. McBreen, C.-P. Grey, D. A. Fischer, Investigation of the Charge Compensation Mechanism on the Electrochemically Li-Ion Deintercalated $Li_{1-x}Co_{1/3}Ni_{1/3}Mn_{1/3}O_2$ Electrode System by Combination of Soft and Hard X-Ray Absorption Spectroscopy, *J. Am. Chem. Soc. 127* (49) (2005) 17479–17487.

(5) Electrodes for Li- Ion Batteries: Materials, Mechanisms and Performance, by L. Monconduit, L. Croguennec and R. Dedryvère First published:30 April 2015 Print ISBN:9781848217218 |Online ISBN:9781119007364 Copyright © 2015 John Wiley & Sons, Inc.

(6) N. Andreu, D. Flahaut, R. Dedryvère, M. Minvielle, H. Martinez, D. Gonbeau, XPS Investigation of Surface Reactivity of Electrode Materials: Effect of the Transition Metal, *ACS Appl. Mater. Interfaces 7* (12) 2015 6629–6636.

(7) G. Vallverdu, M. Minvielle, N. Andreu, D. Gonbeau, I. Baraille, First Principle Study of the Surface Reactivity of Layered Lithium Oxides $LiMO_2$ (M = Ni, Mn, Co), *Surf. Sci. 649 (2016)* 46–55.

(8) L. Dahéron, H. Martinez, R. Dedryvère, I. Baraille, M. Ménétrier, C. Denage, C. Delmas, D. Gonbeau, Surface Properties of $LiCoO_2$ Investigated by XPS Analyses and Theoretical Calculations, *J. Phys. Chem. C* 113 (14) (2009) 5843-5852.

(9) L. Daheron, R. Dedryvere, H. Martinez, D. Flahaut, M.Menetrier, C. Delmas, D. Gonbeau, Possible Explanation for the Efficiency of Al-Based Coatings on $LiCoO_2$: Surface Properties of $LiCo_{1-x}Al_xO_2$ Solid Solution, Chem. Mater. 21 (2009) 5607–5616.

(10) N. Andreu, I. Baraille, H. Martinez, R. Dedryvère, M. Loudet, D. Gonbeau, New Investigations on the Surface Reactivity of Layered Lithium Oxides, *J. Phys. Chem. C 116* (38) (2012) 20332–20341.

(11) A. Quesne-Turin, D. Flahaut, L. Croguennec, G. Vallverdu, J. Allouche, Y. Charles-Blin, J.-N. Chotard, M. Ménétrier, I. Baraille, Surface Reactivity of Li_2MnO_3: First-Principles and Experimental Study, *ACS Appl. Mater. Interfaces 9* (50) (2017) 44222–44230.

(12) A. Quesne-Turin, G. Vallverdu, D. Flahaut, J. Allouche, L. Croguennec, M. Ménétrier, I. Baraille, Morphology and Surface Reactivity Relationship in the $Li_{1+x}Mn_{2-X}O_4$ Spinel with x = 0.05 and 0.10: A Combined First-Principle and Experimental Study, *ACS Appl. Mater. Interfaces 9* (51) (2017) 44922–44930.

(13) W. Tang, H. Kanoh, X. Yang, K. Ooi, Preparation of Plate-Form Manganese Oxide by Selective Lithium Extraction from Monoclinic Li_2MnO_3 under Hydrothermal Conditions, *Chem. Mater. 12* (11) (2000) 3271–3279.

(14) H. Koga, L. Croguennec, M. Ménétrier, P. Mannessiez, F. Weill, C. Delmas, Different Oxygen Redox Participation for Bulk and Surface: A Possible Global Explanation for the Cycling Mechanism of $Li_{1.20}Mn_{0.54}Co_{0.13}Ni_{0.13}O_2$, *J. Power Sources* 2*36 (2013)* 250–258.

(15) M. Sathiya, G. Rousse, K. Ramesha, C.-P. Laisa, H. Vezin, M. T. Sougrati, M. L. Doublet, D. Foix, D. Gonbeau, W. Walker, Reversible Anionic Redox Chemistry in High-Capacity Layered-Oxide Electrodes, *Nat Mater 12* (9) (2013) 827–835.

(16) D. Foix, M. Sathiya, E. McCalla, J. M. Tarascon, D. Gonbeau, X-Ray Photoemission Spectroscopy Study of Cationic and Anionic Redox Processes in High-Capacity Li-Ion Battery Layered-Oxide Electrodes, *J. Phys. Chem. C* 1*20* (2) (2016) 862–874.

(17) A. Boulineau, L. Croguennec, C. Delmas, F. Weill, Structure of Li_2MnO_3 with Different Degrees of Defects, *Solid State Ion. 180* (40) (2010) 1652–1659.

(18) A. S. Menon, D. O. Ojwang, T. Willhammar, V. K. Peterson, K. Edström, C. P. Gomez, W. R. Brant, Influence of Synthesis Routes on the Crystallography, Morphology, and Electrochemistry of Li_2MnO_3, ACS Appl. Mater. Interfaces 12 (5) (2020) 5939–5950.

(19) T. Matsunaga, H. Komatsu, K. Shimoda, T. Minato, M. Yonemura, T. Kamiyama, S. Kobayashi, T. Kato, T. Hirayama, Y. Ikuhara, H. Arai, Y. Ukyo, Y. Uchimoto, Z. Ogumi, Dependence of Structural Defects in Li_2MnO_3 on Synthesis Temperature, Chem. Mater.28 (2016) 4143−4150.

(20) A. Boulineau, L. Croguennec, C. Delmas, F. Weill, Reinvestigation of Li_2MnO_3 Structure: Electron Diffraction and High Resolution TEM, *Chem. Mater. 21* (18) (2009) 4216–4222.

(21) M. Reynaud, J. Serrano-Sevillano, A. Saracibar, T. Altantzis, S. Bals, G. van Tendeloo, J. Rikarte, J. Rodrigues-Carvajal, M. Casas-Cabanas, Investigation of planar defects in electrode materials using FAULTS, Acta. Crystal. A, 74 (2018) E87-E87.

(22) M. M. Treacy, J. M. Newsam, M. W. A. Deem, General Recursion Method for Calculating Diffracted Intensities from Crystals Containing Planar Faults, *Proc. R. Soc. Lond. Math. Phys. Eng. Sci. 433* (1889) (1995) 499–520.

(23) T. Yokoyama, A. Imanishi, S. Terada, H. Namba, Y. Kitajima, T. Ohta, Electronic Properties of SO_2 Adsorbed on Ni(100) Studied by UPS and O K-Edge NEXAFS, *Surf. Sci. 334* (1) (1995) 88–94.

(24) S. P. Mehandru, A. B. Anderson, Adsorption of O_2, SO_2, and SO_3, on Nickel Oxide Mechanism for Sulfate Formation, *J. Electrochem. Soc. 133* (4) (1986) 828–832.

(25) G. Kresse, J. Hafner, Ab Initio Molecular Dynamics for Liquid Metals, *Phys. Rev. B 47* (1) (1993) 558–561.

(26) G. Kresse, J. Furthmüller, Efficiency of Ab-Initio Total Energy Calculations for Metals and Semiconductors Using a Plane-Wave Basis Set, *Comput. Mater. Sci. 6* (1) (1996) 15–50.

(27) J. P. Perdew, A. Ruzsinszky, G. I. Csonka, O. A. Vydrov, G. E. Scuseria, L. A. Constantin, X. Zhou, K. Burke, Restoring the Density-Gradient Expansion for Exchange in Solids and Surfaces, *Phys. Rev. Lett. 100* (13) (2008) 136406.

(28) G. Kresse, D. Joubert, From Ultrasoft Pseudopotentials to the Projector Augmented-Wave Method, *Phys. Rev. B 59* (3) (1999) 1758–1775.

(29) G. Henkelman, A. Arnaldsson, H. Jónsson, A Fast and Robust Algorithm for Bader Decomposition of Charge Density, *Comput. Mater. Sci. 36* (3) (2006) 354–360.

(30) S. L. Dudarev, G. A. Botton, S. Y. Savrasov, C. J. Humphreys, A. P. Sutton, Electron-Energy-Loss Spectra and the Structural Stability of Nickel Oxide: An LSDA+U Study, *Phys. Rev. B 57* (3) (1998) 1505–1509.

(31) F. Zhou, M. Cococcioni, C. Marianetti, D. Morgan, G. Ceder, First-Principles Prediction of Redox Potentials in Transition-Metal Compounds with LDA+U, *Phys. Rev. B 70* (23) (2004) 235121.

(32) Y. Koyama, I. Tanaka, M. Nagao, R. Kanno, R. First-Principles Study on Lithium Removal from Li_2MnO_3, *J. Power Sources 189* (1) (2009) 798–801.

(33) Y. Koyama, H. Arai, I. Tanaka, Y. Uchimoto, Z. Ogumi, Defect Chemistry in Layered Li M O $_2$ (M = Co, Ni, Mn, and Li $_{1/3}$ Mn $_{2/3}$) by First-Principles Calculations, *Chem. Mater. 24* (20) (2012) 3886–3894.

(34) G. Lang, Strukturvergleiche an Ternären Und Quarternären Oxiden. *Z. Für Anorg. Allg. Chem. 348* (5–6) (1966) 246–256.

(35) J. Bréger, M. Jiang, N. Dupré, Y. S. Meng, Y. Shao-Horn, G. Ceder, C. P. Grey, High-Resolution X-Ray Diffraction, DIFFaX, NMR and First Principles Study of Disorder in the

Li_2MnO_3–$Li[Ni_{1/2}Mn_{1/2}]O_2$ Solid Solution. *J. Solid State Chem.* 1*78* (9) (2005) 2575–2585.

(36) G. C. Allen, S. J. Harris, J. A. Jutson, J. M. Dyke, A study of a Number of Mixed Transition Metal Oxide Spinels using X-ray Photoelectron Spectroscopy, Appl. Surf. Sci. 37 (1989) 111−134.

(37) Wood, K. N.; Teeter, G. XPS on Li-Battery-Related Compounds: Analysis of Inorganic SEI Phases and a Methodology for Charge Correction. *ACS Appl. Energy Mater.* **2018**, *1* (9), 4493–4504. https://doi.org/10.1021/acsaem.8b00406.

(38) Y. Shin, K. A. Persson, Surface Morphology and Surface Stability against Oxygen Loss of the Lithium-Excess Li_2MnO_3 Cathode Material as a Function of Lithium Concentration, *ACS Appl. Mater. Interfaces 8* (38) (2016) 25595–25602.

(39) C. Guimon, A. Gervasini, A. Auroux, XPS Study of the Adsorption of SO_2 and NH_3 over Supported Tin Dioxide Catalysts Used in De-NOx Catalytic Reaction. *J. Phys. Chem. B 105* (42) (2001) 10316–10325.